Metal clad waveguide (MCWG) based imaging using a high numerical aperture microscope objective

Thomas Söllradl, Frederic Banville, Vincent Chabot, Michael Canva, Michel Grandbois, Paul Charette

Research Article | Vol. 25, No. 3 | 6 Feb 2017 | OPTICS EXPRESS 1666

Optics EXPRESS

Metal clad waveguide (MCWG) based imaging using a high numerical aperture microscope objective

THOMAS SÖLLRADL,[1,2,3] FREDERIC A. BANVILLE,[1,2] VINCENT CHABOT,[1,2] MICHAEL CANVA,[1,2] MICHEL GRANDBOIS,[1,3,4] AND PAUL G. CHARETTE[1,2,*]

[1]*Laboratoire Nanotechnologies Nanosystèmes (LN2)- CNRS UMI-3463, Université de Sherbrooke, Sherbrooke, Canada*
[2]*Institut Interdisciplinaire d'Innovation Technologique (3IT), Université de Sherbrooke, Sherbrooke, Canada*
[3]*Département de Pharmacologie et Physiologie, Université de Sherbrooke, Sherbrooke, Canada*
[4]*Institut de Pharmacologie de Sherbrooke, Sherbrooke, Canada*
[*]*Paul.G.Charette@USherbrooke.ca*

Abstract: Evanescent-field based methods such as surface plasmon resonance (SPR) have been used very effectively for label-free imaging of microscopic biological material in close proximity to a sensing surface. However, the shallow probing depth of SPR (typically less than ~200 nm) can be problematic when imaging relatively thick biological objects such as cells or bacteria. In this paper, we demonstrate how metal-clad waveguides (MCWG) can be used to achieve deeper probing depth compared to SPR while maintaining good imaging spatial resolution. Comparative numerical simulations of imaging spatial resolution versus probing depth are shown for a number of common SPR, long-range SPR, and MCWG configurations, demonstrating that MCWG offer the best compromise between resolution and depth for imaging thick biological objects. Experimental results of synthetic target and live cell imaging are shown that validate the numerical simulations and demonstrate the capabilities of the method.

OCIS codes: (240.6680) Surface plasmons; (110.0110) Imaging systems; (110.0180) Microscopy; (130.2755) Glass waveguides.

References and links

1. E. Kretschmann and H. Raether, "Radiative decay of non-radiative surface plasmons excited by light," Z. Naturforsch. B **23**, 2135–2136 (1968).
2. A. Otto, "Excitation of nonradiative surface plasma waves in silver by the method of frustrated total reflection," Z. Phys. **216**(4), 398–410 (1968).
3. J. Homola, "Present and future of surface plasmon resonance biosensors," Anal. Bioanal. Chem. **377**(3), 528–539 (2003).
4. A. Sereda, J. Moreau, M. Canva, and E. Maillart, "High performance multi-spectral interrogation for surface plasmon resonance imaging sensors," Biosens. Bioelectron. **54**, 175–180 (2014).
5. L. Laplatine, L. Leroy, R. Calemczuk, D. Baganizi, P. N. Marche, Y. Roupioz, and T. Livache, "Spatial resolution in prism-based surface plasmon resonance microscopy," Opt. Express **22**(19), 22771–22785 (2014).
6. B. Huang, F. Yu, and R. N. Zare, "Surface plasmon resonance imaging using a high numerical aperture microscope objective," Anal. Chem. **79**(7), 2979–2983 (2007).
7. F. A. Banville, T. Söllradl, P.-J. Zermatten, M. Grandbois, and P. G. Charette, "Improved resolution in SPR and MCWG microscopy by combining images acquired with distinct mode propagation directions," Opt. Lett. **40**(7), 1165–1168 (2015).
8. D. J. Kim and D. Kim, "Subwavelength grating-based nanoplasmonic modulation for surface plasmon resonance imaging with enhanced resolution," J. Opt. Soc. Am. B **27**(6), 1252 (2010).
9. Y. Yanase, T. Hiragun, S. Kaneko, H. J. Gould, M. W. Greaves, and M. Hide, "Detection of refractive index changes in individual living cells by means of surface plasmon resonance imaging," Biosens. Bioelectron. **26**(2), 674–681 (2010).
10. W. Wang, S. Wang, Q. Liu, J. Wu, and N. Tao, "Mapping single-cell-substrate interactions by surface plasmon resonance microscopy," Langmuir **28**(37), 13373–13379 (2012).
11. A. W. Peterson, M. Halter, A. Tona, and A. L. Plant, "High resolution surface plasmon resonance imaging for single cells," BMC Cell Biol. **15**(1), 35 (2014).

#282907 http://dx.doi.org/10.1364/OE.25.001666
Journal © 2017 Received 15 Dec 2016; accepted 15 Jan 2017; published 23 Jan 2017

Optics EXPRESS

12. P. Kanchanawong, G. Shtengel, A. M. Pasapera, E. B. Ramko, M. W. Davidson, H. F. Hess, and C. M. Waterman, "Nanoscale architecture of integrin-based cell adhesions," Nature **468**(7323), 580–584 (2010).
13. V. Chabot, Y. Miron, M. Grandbois, and P. G. Charette, "Long range surface plasmon resonance for increased sensitivity in living cell biosensing through greater probing depth," Sens. Actuators B Chem. **174**, 94–101 (2012).
14. R. Méjard, J. Dostálek, C.-J. Huang, H. Griesser, and B. Thierry, "Tuneable and robust long range surface plasmon resonance for biosensing applications," Opt. Mater. **35**(12), 2507–2513 (2013).
15. O. Krupin, H. Asiri, C. Wang, R. N. Tait, and P. Berini, "Biosensing using straight long-range surface plasmon waveguides," Opt. Express **21**(1), 698–709 (2013).
16. A. W. Wark, H. J. Lee, and R. M. Corn, "Long-range surface plasmon resonance imaging for bioaffinity sensors," Anal. Chem. **77**(13), 3904–3907 (2005).
17. I. P. Kaminow, W. L. Mammel, and H. P. Weber, "Metal-clad optical waveguides: analytical and experimental study," Appl. Opt. **13**(2), 396–405 (1974).
18. N. Skivesen, R. Horvath, and H. C. Pedersen, "Optimization of metal-clad waveguide sensors," Sens. Actuators B Chem. **106**(2), 668–676 (2005).
19. L. Convert, V. Chabot, P. J. Zermatten, R. Hamel, Jr., J. P. Cloarec, R. Lecomte, V. Aimez, and P. G. Charette, "Passivation of KMPR microfluidic channels with bovine serum albumin (BSA) for improved hemocompatibility characterized with metal-clad waveguides," Sens. Actuators B Chem. **173**, 447–454 (2012).
20. W. Choi, C. Fang-Yen, K. Badizadegan, S. Oh, N. Lue, R. R. Dasari, and M. S. Feld, "Tomographic phase microscopy," Nat. Methods **4**(9), 717–719 (2007).
21. L. Convert, V. Aimez, P. G. Charette, and R. Lecomte, "Rapid prototyping of integrated microfluidic devices for combined radiation detection and plasma separation," in *MNRC 2008 - 1st Microsystems and Nanoelectronics Research Conference* (IEEE, 2008), pp. 105–108.
22. J. Moreau, J.-P. Cloarec, P. Charette, M. Goossens, M. Canva, and T. Vo-Dinh, "Chapter 7. Surface Plasmon Resonance Imaging Sensors: Principle, Development, and Biomedical Applications—Example of Genotyping," in *Biomedical Diagnostics*, T. Vo-Dinh, ed. (CRC Press, 2014), pp. 199–264.
23. P. B. Johnson and R. W. Christy, "Optical constants of the noble metals," Phys. Rev. B **6**(12), 4370–4379 (1972).
24. M. Daimon and A. Masumura, "Measurement of the refractive index of distilled water from the near-infrared region to the ultraviolet region," Appl. Opt. **46**(18), 3811–3820 (2007).
25. M. K. Yang, R. H. French, and E. W. Tokarsky, "Optical properties of Teflon® AF amorphous fluoropolymers," J. Micro/Nanolithography **7**, 33010 (2008).
26. H. B. Pyo, Y. B. Shin, M. G. Kim, and H. C. Yoon, "Multichannel surface plasmon resonance imaging and analysis of micropatterned self-assembled monolayers and protein affinity interactions," Langmuir **21**(1), 166–171 (2005).
27. Z. Salamon and G. Tollin, "Optical anisotropy in lipid bilayer membranes: coupled plasmon-waveguide resonance measurements of molecular orientation, polarizability, and shape," Biophys. J. **80**(3), 1557–1567 (2001).
28. Z. Salamon, H. A. Macleod, and G. Tollin, "Coupled plasmon-waveguide resonators: a new spectroscopic tool for probing proteolipid film structure and properties," Biophys. J. **73**(5), 2791–2797 (1997).
29. B. H. Ong, X. Yuan, S. C. Tjin, J. Zhang, and H. M. Ng, "Optimised film thickness for maximum evanescent field enhancement of a bimetallic film surface plasmon resonance biosensor," Sens. Actuators B Chem. **114**(2), 1028–1034 (2006).
30. T. Liebermann and W. Knoll, "Surface-plasmon field-enhanced fluorescence spectroscopy," Colloids Surfaces A Physicochem. Eng. Asp. **171**(1-3), 115–130 (2000).
31. J.-F. Bryche, R. Gillibert, G. Barbillon, P. Gogol, J. Moreau, M. Lamy de la Chapelle, B. Bartenlian, and M. Canva, "Plasmonic enhancement by a continuous gold underlayer: application to SERS sensing," Plasmonics **11**(2), 601–608 (2016).
32. K.-S. Ou, H.-Y. Yan, and K.-S. Chen, "Mechanical characterization of KMPR by nano-indentation for MEMS applications," Strain **44**(3), 267–271 (2008).
33. V. M. Blanco Carballo, J. Melai, C. Salm, and J. Schmitz, "Moisture resistance of SU-8 and KMPR as structural material for integrated gaseous detectors," in *11th Annual Workshop on Semiconductor Advances for Future Electronics and Sensors* (Elsevier, 2008), pp. 395–398.
34. B. Rothenhäusler and W. Knoll, "Surface plasmon interferometry in the visible," Appl. Phys. Lett. **52**(19), 1554–1556 (1988).
35. E. M. Yeatman, "Resolution and sensitivity in surface plasmon microscopy and sensing," Biosens. Bioelectron. **11**(6-7), 635–649 (1996).
36. V. Yashunsky, V. Lirtsman, M. Golosovsky, D. Davidov, and B. Aroeti, "Real-time monitoring of epithelial cell-cell and cell-substrate interactions by infrared surface plasmon spectroscopy," Biophys. J. **99**(12), 4028–4036 (2010).

1. Introduction

Ever since its experimental demonstration by Otto and Kretschmann [1,2], surface plasmon resonance (SPR) has become a valuable label-free sensing approach with a broad range of

Optics EXPRESS

applications in the fields of chemistry, engineering, and biology. The basis for SPR sensing is that TM-polarized light can be guided by a surface-bound mode at the interface between a metal and a dielectric, where the dielectric is the sensing medium (a gas or a liquid). Although there is a simple closed-form solution to determine the effective index for this guided "surface plasmon mode" [3], it can also be obtained by solving the transcendental equation for guided TM modes in a planar waveguide derived from Maxwell's equations with a null core thickness. As with guided modes in a conventional dielectric waveguide, light can be coupled to the surface plasmon mode in a number of ways, with prism-based systems being the most common (optical tunneling via total internal reflection). Since absorption of visible and near-IR light in most metals is high, the surface plasmon mode is highly lossy. Indeed, these losses in the metal are at the heart of the resonant nature of plasmonics-based sensors, where coupling conditions can be adjusted such that virtually all light injected into the system at the operating point is absorbed (critical coupling). As is typical for resonance-based guided-mode systems, critical coupling conditions are very sensitive to the waveguide physical parameters. As a result, minute chemical or physical changes that perturb the refractive index of the sensing media above the metal surface will detune the system from resonance and be observable either as intensity variations of the reflected light when operating at fixed incidence angle and wavelength, or as a change in incidence angle and/or wavelength of the critical coupling conditions [4]. Owing to the evanescent profile of the electric field in the dielectric, SPR is sensitive to refractive index changes in close proximity to the metal surface. The distance from the interface (normal to the direction of mode propagation) over which the mode amplitude decreases by 1/e of its value at the interface is termed the "penetration depth", typically below 200 nm for visible wavelengths and noble metals [3], and is commonly used as a measure of effective sensing depth.

In surface plasmon resonance imaging (SPRI), a 2D photodetector such as a CCD camera is used to monitor changes in reflectivity so that refractive index perturbations in the dielectric medium can be spatially resolved in the plane of the metal/dielectric interface, with most systems using a prism for input/output light coupling. Due to the physical size of the prism, the imaging optics typically have modest resolving power as they are necessarily based on long working distance low numerical apertures objectives. In practice, however, spatial resolution in prims-based SPRI is normally well above the diffraction limit of the optics due to aberrations and distortion resulting from passage of light through the prism [5], typically in the order of ten(s) of microns. To overcome these limitations, a high-numerical aperture microscope objective can be used instead to directly couple in/out of the surface plasmon mode [6]. Such systems, however, reveal an additional impediment to spatial resolution in SPRI. The amplitude of the guided surface plasmon mode decreases exponentially in the direction of propagation due to losses in the metal, where the distance over which the mode energy decreases by 1/e is termed the "propagation distance" or "attenuation length". In high-resolution SPRI, this finite attenuation distance causes cross-talk between neighboring pixels along the direction of mode propagation, effectively blurring the images along that axis and resulting in a spatial resolution imbalance between the two orthogonal axes in the image plane. Though this effect can be slightly noticeable in prism-based systems, it is a significant problem in high magnification microscope objective-based systems. This effect can be reduced to some extent by using shorter wavelength excitation [6], combining images acquired with distinct mode propagation directions [7], or surface nanostructuring [8].

There is increasing interest in surface-based label-free imaging of relatively large microscopic objects such as bacteria and cells [9–11]. Conventional "short-range" SPRI systems are very effective for studying cell-substrate adhesion sites, structures that are located within the first hundred nanometers of the cell body above the sensor surface [12]. There is, however, a demand to study other cytoskeletal components located higher up in the cell body such as actin (> 160 nm) and intracellular organelles (> 200 nm), requiring deeper probing depths into the dielectric medium than conventional "short-range" SPRI systems can deliver.

Optics EXPRESS

To increase penetration depth, longer wavelengths in the near-IR can be used with SPRI. Alternatively, so-called "long-range" SPR (LR-SPR) can be used [13–16], as discussed below. In both cases, however, imaging resolution along the direction of mode propagation deteriorates commensurately with penetration depth due to the increased attenuation distance.

As demonstrated in this paper, a third and very flexible approach to increase penetration depth while more effectively controlling attenuation distance involves the use of *metal-clad waveguides* (MCWG): dielectric core waveguides with metal film claddings on one or more sides) [17,18]. In fact, unbeknownst to many in the plasmonics community, SPR is actually a special case of this broader class of waveguides: conventional propagating SPR devices based on a single metal/dielectric interface can be considered as MCWG waveguides that support a single TM surface mode, i.e. a MCWG with a null core thickness.

In this work, we present a MCWG-based imaging system based on a high numerical aperture objective. Numerical simulation results comparing the estimated performance of the MCWG-based system compared to SPR and LR-SPR are shown. The system's imaging capabilities are characterized using synthetic structures and living cells.

2. Metal-clad vs plasmonic waveguide modes: numerical simulations

This section compares the expected performance of sensor chip structures based on conventional (short-range) SPR, long-range SPR (LR-SPR), and metal-clad waveguides (MCWG) using four performance metrics: refractive index measurement sensitivity and dynamic range, attenuation length (spatial resolution in the imaging plane), and penetration depth into the dielectric (imaging depth). Since the objective is to probe deeply into the dielectric, the "bulk" definition of sensitivity is used (maximum reflectivity change as a function of refractive index change in the dielectric volume) as opposed to sensitivity defined with respect to surface biolayer (adlayer) thickness or surface coverage.

These numerical analyses were conducted using modal analysis methods (also known as mode solvers or eigen mode expansion) based on solving Maxwell's equations with finite differences on a rectangular grid in the plane perpendicular to the direction of propagation, using the FIMMWAVE software package (Photon Design, UK). This type of analysis yields the complete description of guided modes supported by the structure (complex effective index of each mode with its full 3D electromagnetic profile). The simulated structures are planar waveguides consisting of thin film stacks of infinite extend in the film plane, sandwiched between two semi-infinite volumes of BK7 glass (bottom) and distilled water (top) modeled by perfectly matched layers (PML). Note that though we measured the dielectric indices of the materials we used with an ellipsometer, the numerical simulations shown below are based on optical properties obtained from the literature and manufacturers so that our results may be reproducible by others. Since the refractive indices for the different materials, most notably metals, may vary significantly according to fabrication conditions, the simulations result shown below will likely differ from actual experimental results. However, the relative performance of the different cases illustrated will remain the same. Hence, these simulations based on materials data from the literature are useful in making informed choices when comparing the relative merits of the cases discussed.

Optics EXPRESS

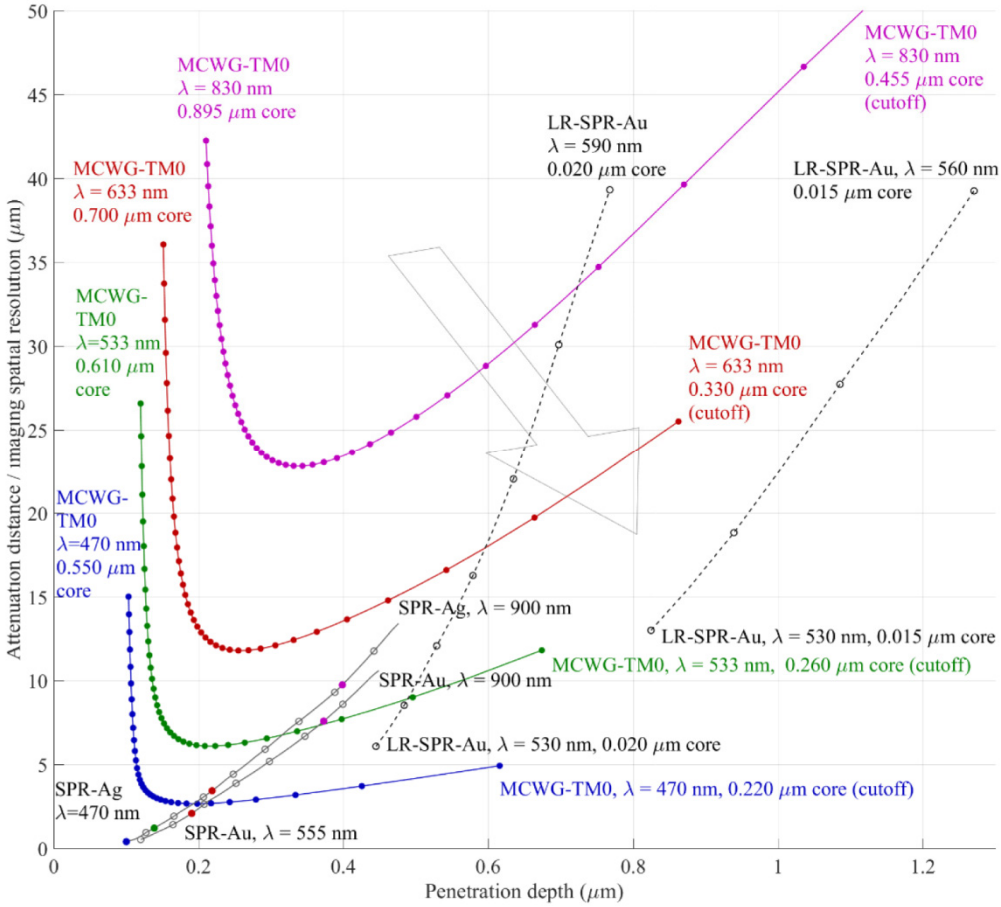

Fig. 1. Mode attenuation distance (imaging spatial resolution) vs penetration depth in the dielectric for MCWG TM0 modes (solid colored lines), SPR (solid gray lines), and LR-SPR (hashed grey lines). The diagonal arrow in the background indicates the direction of improving performance for imaging of thick objects such as cells, i.e. decreasing attenuation distance (better resolution) and increasing penetration depth. Data calculated using FIMMWAVE. MCWG: TM0 modes (colored curves) at wavelengths of 470 nm, 533 nm, 633 nm, and 830 nm, over a range of KMPR core thicknesses. Markers indicate core thickness intervals of 10 nm, starting at cutoff (thinnest core supporting a guided mode, rightmost point on each plot); SPR: Au/water and Ag/water interface surface modes over a range of wavelengths (Au: 555 nm – 900 nm, Ag: 470 nm - 900 nm). Black markers indicate wavelength intervals of 50 nm, while colored markers indicate the wavelengths corresponding to the four MCWG curves (470 nm, 533 nm, 633 nm, 830 nm); LR-SPR: symmetric mode in a Teflon/Au/water stack over a range of relevant wavelengths (15 nm Au core: 530 nm to 560 nm, 20 nm Au core: 530 nm to 590 nm). Markers indicate wavelength intervals of 10 nm;

MCWG devices have been shown by us [19] and others [18] to have superior bulk sensitivity compared to SPR. Though LR-SPR can have slightly better bulk sensitivity than MCWG [19], this comes at the expense of a much narrower dynamic range, which is an important parameter for cell imaging since the intra- and extra-cellular media can have significant refractive index differences ($n \approx 1.33$ vs. $n = 1.36$ - 1.39 [20], respectively). Based on measurement sensitivity and dynamic range metrics, therefore, MCWG-based devices are strong candidates for cell imaging.

The attenuation distance (imaging spatial resolution in the plane) and penetration depth are two metrics that are in direct competition. Figure 1 illustrates this trade-off for three waveguide constructs (MCWG, SPR, LR-SPR) based on Au and Ag films, the most

Optics EXPRESS

commonly used metals. Numerical simulation results of attenuation distance versus penetration depth are plotted for: (1) MCWG TM0 modes (colored lines) for a range of core thicknesses at four typical wavelengths (470 nm, 532 nm, 632 nm, and 830 nm). The dielectric core material of the MCWG is KMPR (MichroChem, USA), a photopolymer similar to SU8 having superior resistance to fissuring during thermal treatment making it a better choice for microfluidics systems [21]. The metal stack between the BK7 substrate and the KMPR core consists of a 3 nm Ni adhesion layer, a 23 nm Ag "main" metal layer and a 5 nm Au passivation layer.

The data for an equivalent MCWG structure with Au as the main metal (Cr/Au metal stack) are not shown as the resulting sensitivity and attenuation distance vs penetration depth trade-off are less advantageous compared to an Ag-based metal stack [22]; (2) SPR modes (solid grey lines) for Au and Ag metal films (including a 3 nm Cr adhesion layer for Au and a 3 nm Ni adhesion layer for Ag); (3) LR-SPR symmetric modes (hashed grey lines) for 15 nm and 20 nm thickness Au cores (NB: simulation data for Ag films are not presented as the resulting much longer attenuation distances are not of practical value for imaging; simulation data for the asymmetric LR-SPR modes are not shown as they are very close to the single-interface SPR modes). The bottom cladding material for the LR-SPR waveguides is Teflon AF1300. In all cases, refractive indices for the metals were taken from Johnson & Christy [23], the Sellmeier equation was used for the refractive index of water [24] and Teflon [25], the Cauchy equation was used for the refractive index of KMPR (coefficients from the product datasheet available on the MicroChem website). The shortest wavelengths considered in the simulations were 450 nm for Ag and 530 nm for Au since losses in these metals at shorter wavelengths reduce measurement sensitivity and dynamic range to very low levels [26]. The longest wavelengths considered are in the near IR (900 nm) which is the practical limit for Si-based imaging devices.

For imaging thick objects such as cells, the optimal operating point is in the lower right area of the figure as indicated by the large diagonal arrow in the background: short attenuation distance (high spatial resolution) and deep penetration. In all cases, the spatial resolution vs penetration depth tradeoff is a function of wavelength: losses in the metals increase with decreasing wavelength thereby shortening the attenuation distance and improving spatial resolution, while penetration depth decreases accordingly. In the cases of LR-SPR and MCWG, the degree of mode confinement is also in play: a thinner core will decrease mode confinement, resulting in deeper probing depth but at the expense of a decrease in spatial resolution due to the accompanying increase in attenuation length (proportionately lower losses in the metal).

Clearly, SPR-based devices are capable of the highest spatial resolution but are limited to relatively shallow probing depths of ~0.4 μm (830 nm excitation wavelength). For deeper probing depths, the best compromise relative to attenuation distance is obtained for MCWG and LR-SPR at short wavelengths. In case of the LR-SPR, however, wavelengths below ~550 nm are close to the practical operating limit for plasmonics with Au where sensitivity is significantly reduced. Conversely, Ag-based devices operate very well at short wavelengths in the visible range. Hence, MCWG-based devices at short wavelengths (470 nm in our case) offer the better tradeoff between achievable resolution and penetration depth for imaging when operated close to the cutoff (thinnest waveguide core supporting a guided mode).

Optics EXPRESS

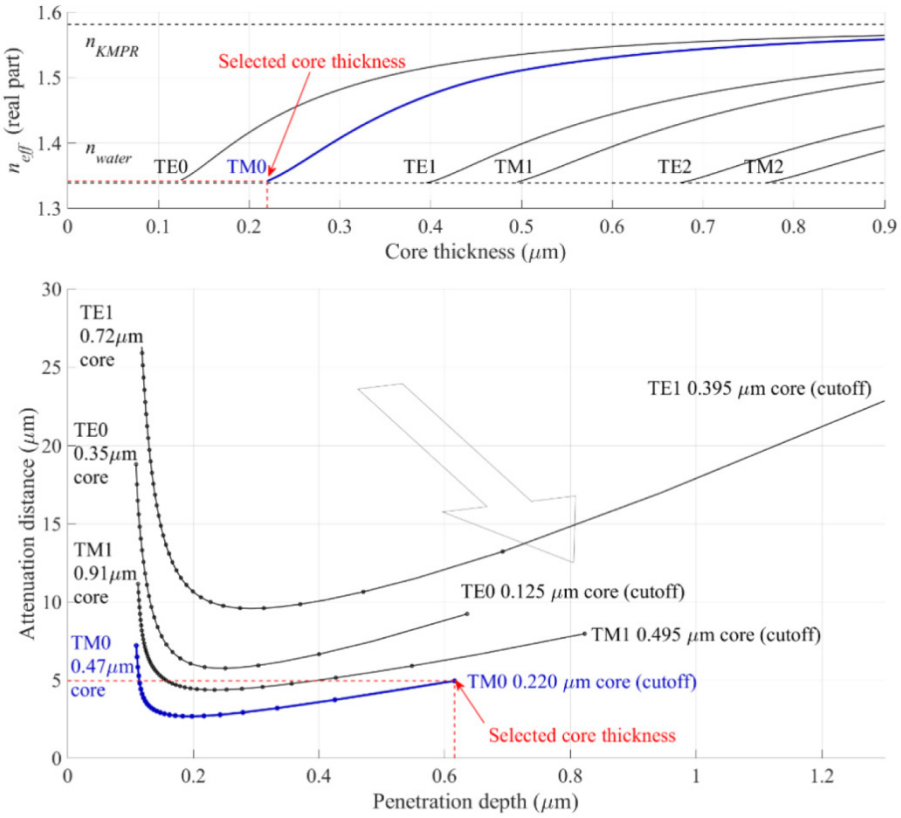

Fig. 2. MCWG modal characteristics at λ = 0.470 nm as a function of core thickness and mode order, waveguide stack: BK7 – Ni(3 nm)/Ag(23 nm)/Au(5 nm) – KMPR - water. The dashed red line indicates the core thickness selected for the experiments (0.220 µm). Plots for the TM0 mode are shown in blue. Data calculated with FIMMWAVE. TOP: mode effective indices (n_{eff}, real part) as a function of core thickness, delimited by the indices of water (cladding with highest index, bottom horizontal dashed line) and KMPR (waveguide core, top horizontal dashed line), i.e.: $n_{water} < \mathrm{Re}\{n_{eff}\} < n_{KMPR}$. BOTTOM: attenuation distance vs penetration depth in the dielectric (water) for modes TE0, TM0, TE1, and TM1 as a function of core thickness - markers indicate core thickness intervals of 0.010 µm. The large diagonal arrow in the background indicates the direction of improving performance for imaging of thick objects, i.e. decreasing attenuation distance (improving resolution) and increasing penetration depth.

Figure 2 shows numerical simulation results at λ = 470 nm illustrating the dependence of the MCWG characteristics on the core layer thickness, starting from the cutoff thickness (thinnest core that will support a guided mode). Figure 2-TOP shows the mode effective indices as a function of core thickness for the first six modes: mode TE0 appears at a core thickness of ~0.13 µm and mode TM0 at a core thickness of ~0.22 µm, followed by the second TE and TM modes at core thicknesses of ~0.40 µm and ~0.50 µm, respectively, etc. Figure 2-BOTTOM shows the attenuation distance versus penetration depth trade-off for the different modes, where markers indicate increments of 10 nm core thickness. Here again, for imaging thick objects such as cells, the optimal operating point is in the lower right area of the figure as indicated by the large diagonal arrow in the background. Clearly, mode TM0 performs best for imaging, followed closely by mode TM1. The higher order TE and TM modes could provide both greater penetration depth and additional physical insight into properties such as optical anisotropy [27].

For the set of experiments presented in this paper, we chose to use mode TM0 in a MCWG with a core thickness of 0.22 µm to operate just above cutoff in order to minimize

Optics EXPRESS

mode confinement and thereby maximize penetration depth of the electric field into the cladding (dotted line in Fig. 2 graphs). The corresponding Ag layer thickness (23 nm) yielding minimum reflectivity at resonance was calculated using the Fresnel equations. According to these simulation results, imaging resolution is ~5 μm and penetration depth ~0.62 μm. The bulk sensitivity for this structure is estimated to be 96 RIU^{-1}.

Figure 3-TOP shows numerical simulations at λ = 470 nm of the normalized electric (LEFT) and magnetic (RIGHT) field intensity profiles, $(|E_z|^2 + |E_y|^2)/|E_0|^2$ and $|H_x|^2/|H_0|^2$, for mode TM0 in the chosen MCWG structure as a function of distance along the z axis (normal to the film plane) from the core/fluid interface at z = 0 μm, where E_0 and H_0 are the incident electric and magnetic field intensities, respectively. As expected for a TM mode, the magnetic field is C^0 continuous at the material boundaries while the electric field is not. Also indicated in the electric field intensity graph is the penetration depth, L_p = 0.62 μm. Since the intensity profiles are normalized with respect to the incident field values, the graphs also indicate the so-called "field enhancement factor" defined as the ratio between the incident field intensity and the maximum field intensity in the fluid occurring at the core/fluid interface (z = 0 μm).

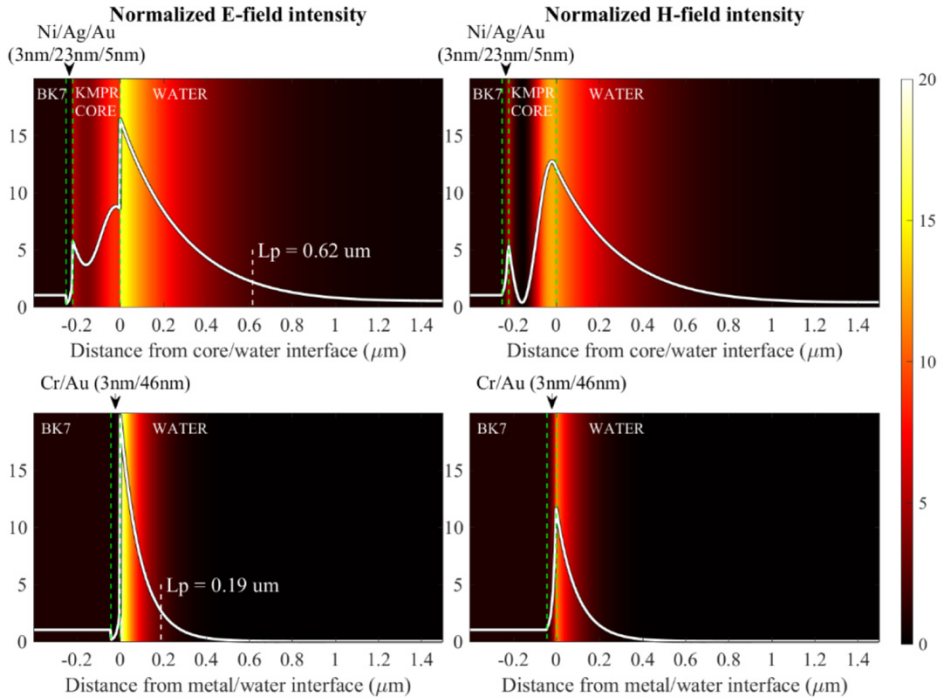

Fig. 3. Electric (LEFT) and magnetic (RIGHT) field intensity profiles, $(|E_z|^2 + |E_y|^2)/|E_0|^2$ and $|H_x|^2/|H_0|^2$, as a function of distance along the z axis (normal to the layer plane) from the fluid/solid interface (z = 0 μm) normalized with respect to the incident field intensities, E_0 and H_0. The L_p markers indicate the "penetration depth" into the fluid (distance from the interface over which the mode amplitude decreases by 1/e of its value at the interface). Background color indicates field intensity. TOP: TM0 mode in the chosen MCWG structure (220 nm KMPR core) at λ = 470 nm. The metal film stack, Ni(3 nm)/Ag(23 nm)/Au(5 nm), is located between the BK7 and KMPR layers. BOTTOM: SPR mode at a Au/water interface at λ = 633 nm. The metal film stack, Cr(3 nm)/Au(46 nm), is located between the BK7 and water layers. Data calculated with FIMMWAVE.

As seen in the figure, the electric field intensity enhancement factor is ~16 × . Note that losses in the Au passivation layer slightly reduce this figure compared to MCWG based on bare Ag films, reported to achieve ~25 × field enhancement [28]. The Ag/Au bimetallic configuration, however, is stable in an aqueous solution (unlike bare Ag) and confers higher sensitivity than Au films alone [29].

Optics EXPRESS

For comparison, Fig. 3-BOTTOM shows the equivalent simulation results for an SPR mode at an Au/water interface at λ = 633 nm, one of the most common SPR sensing configurations. Relative to the MCWG TM0 mode (TOP), the penetration depth of the SPR mode is about 1/3 (shallower sensing depth), the propagation distance is about 1/2 (higher imaging spatial resolution, see Fig. 1), while the field enhancement factor is of the same order. Note that for MCWG and "propagating" SPR modes (as opposed to localized plasmonic modes), the notion of "field enhancement" must be interpreted with care as it is highly dependent on the thickness of the metal layer. Indeed, by increasing/decreasing the metal layer thickness in the numerical simulations by a few nm, the field enhancement factor could be made to vary by as much as 50%. Hence, estimated values of field enhancement in this case must be interpreted somewhat qualitatively given practical layer deposition accuracy. Nevertheless, a high field enhancement factor is desirable as it leads to increased signal levels in surface plasmon enhanced fluorescence (SPEF) and surface-enhanced Raman spectroscopy (SERS) [30,31].

3. Instrumentation setup

The optical setup used in our experiments is based on a design first proposed by Huang *et al.* [6] for high-resolution SPRI. As shown in Fig. 4, light from a 17.2 mW fiber-coupled LED centered at 470 nm (M470F3, Thorlabs, USA) passes through a collimating lens followed by a beam-expander (10X BE10M-A, Thorlabs, USA) and is focused into the back focal plane of a high numerical aperture objective (63x, NA = 1.46, Carl Zeiss, Germany). As a result, light incident onto, and reflected from, the backside of the MCWG chip is collimated. The low-coherence LED source reduces interference artifacts and its spectral bandwidth is restricted by a bandpass filter (FB470-10, FWHM = 10 nm, Chroma Technology, USA). The light reflected from the backside of the chip is collected back through the objective where the orthogonal polarizations are imaged by separate CCD cameras (Guppy F-146B, Allied Vision Tech., USA) via a polarizing beamsplitter.

The lateral translation, *d(x,y)*, of the focal spot from the origin in the back focal plane of the objective determines the angle of incidence, θ_i, of the light onto the back surface of the MCWG chip. For *d(x,y)* sufficiently large, light will be incident onto the sample at an angle greater than the angle of total internal reflection at the KMPR/fluid interface and guided modes in the waveguide on the topside of the chip can be excited by optical tunneling through the metal film, as with a conventional prism-based system. The collimating lens / beam expander / focusing lens subsystem is mounted on a linear scanning stage (17DRV114, CVI Melles-Griot, USA) which allows for arbitrary 2D positioning of the focused spot in the back focal plane of the objective. For example, by moving the spot in a circle of constant radius in the *xy* plane, guided modes of constant effective indices can be excited in the waveguide layer along any direction.

Optics EXPRESS

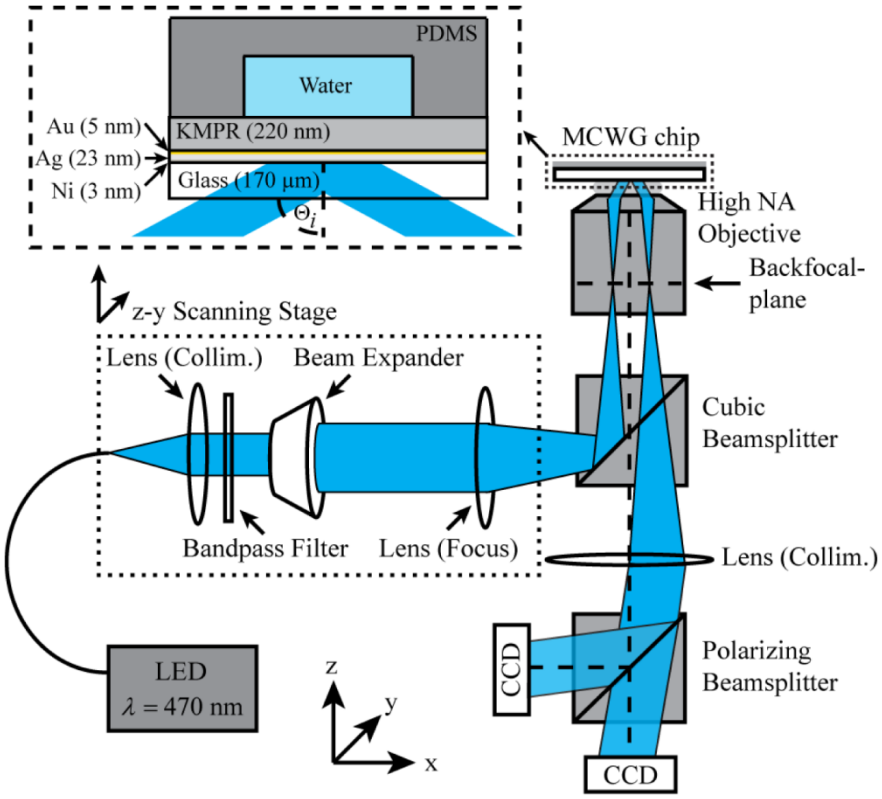

Fig. 4. Schematic diagram of the imaging system based on a high numerical aperture objective. The inset shows the MCWG chip structure: BK7 glass – Ni(3 nm)/Ag(23 nm)/Au(5 nm) – KMPR(220 nm). A PDMS microfluidic channel is patterned atop the KMPR.

The MCWG chips (Fig. 4 inset) were fabricated on 170 µm thick BK7 glass cover slips (Fisher Scientific, USA). After a solvent cleaning (2-propanol, acetone and water, 3 min sonication per step), a 3 nm Ni adhesion layer was deposited by evaporation, followed by a 23 nm Ag layer and a 5 nm Au layer to passivate the silver for use in aqueous media. KMPR films (KMPR 1005, 15% dilution with SU8 thinner, MicroChem, USA) were spin-coated on top of the metal layer. The epoxy-based photopolymer resin KMPR 1005 was chosen as the core material for its superior mechanical stability and moisture resistance compared to other commonly used resins such as SU8 [32,33]. After a soft bake (100 °C, 2 min), samples were exposed to UV light (Model 200, OAI, USA) for 60 sec. (900 mJ/cm^2, no filter), followed by an annealing on a hot plate (100 °C, 2 min) and hard-baked (180 °C, 3 hours) to stabilize the KMPR layer. KMPR thickness was verified by ellipsometry (Alpha_SE, J.A. Woollam Co.). PDMS fluid channels were patterned atop the KMPR. The experimental results presented in the next section were obtained using a typical sensor chip with a KMPR thickness of 219.4 ± 0.3 nm.

4. Experimental Results and Discussion

4.1 Lateral imaging resolution

To experimentally characterize the lateral imaging resolution of our MCWG–based imaging system, the PDMS fluid channel wall boundaries were imaged at λ = 470 nm with the microscope system using two orthogonal light propagation directions, as shown in Fig. 5. The light input/output coupling angle was selected for optimal coupling of the TM0 mode into water.

Optics EXPRESS

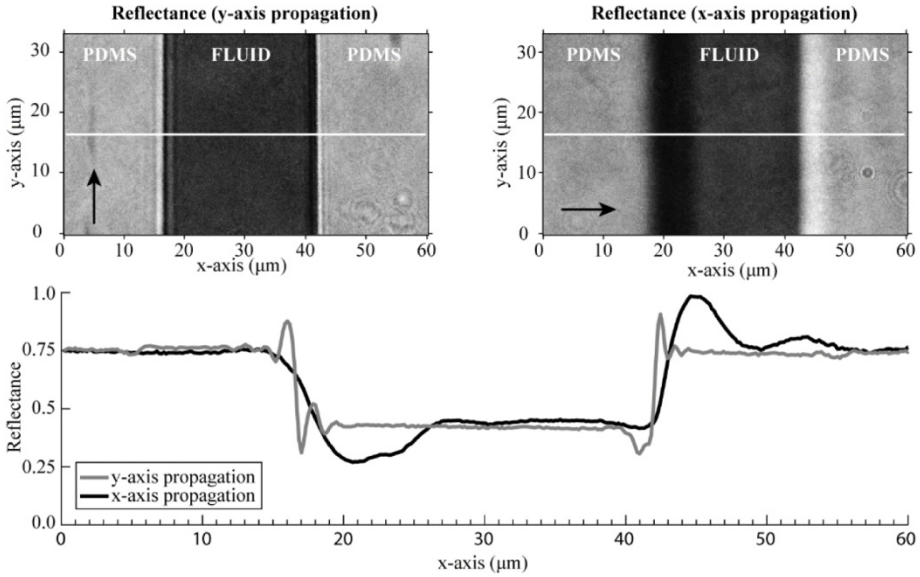

Fig. 5. Typical pair of reflectivity images acquired with the microscope from two orthogonal directions of light propagation using the MCWG chip structure, where the back arrows indicate the direction of light propagation, clearly illustrating the resolution imbalance between the two axes in the plane. The angle of incidence was selected for maximum coupling of the TM0 mode into water at $\lambda = 470$ nm: the light grey zones in the images correspond to PDMS and the central dark grey zones to water. TOP-LEFT: image acquired with light propagating along the *y* axis. TOP-RIGHT: image acquired with light propagating along the *x* axis. BOTTOM: *x*-axis line profiles from both images (white horizontal lines across the top two images). The exponential profile and oscillations at the PDMS/water boundaries that are clearly seen in the *x*-axis propagation profile are due to the finite attenuation distance.

Figure 5 shows two typical reflectivity images acquired with light propagating along the *y* axis (TOP-LEFT) and *x* axis (TOP-RIGHT) in the film plane. As seen in the images, the water/PDMS boundary is sharp for light propagating parallel to the edge but blurred for light propagating perpendicular to the edge, as expected. Line profiles for both images are shown in Fig. 5-BOTTOM. The exponential decay profile and oscillations at the PDMS/water boundaries that are clearly seen in the *x*-axis propagation profile are due to the finite attenuation distance described earlier and have been observed by others [34]. The oscillation period (~7.4 μm) and attenuation distance (exponent of the exponential decay profile:~5 μm) calculated from the line profile are in close agreement with the theoretical predictions from our modeling results (6.8 μm and 4.9 μm, respectively) and similar work in the literature [35]. This phenomenon is the main resolution limitation along the axis of light propagation, whereas resolution along the axis perpendicular to light propagation is ultimately limited by diffraction. Note that narrow fringes can also be seen in the y-axis propagation image parallel to the channel wall boundaries: they are most likely due to imperfect collimation by the light injection optics.

4.2 Imaging depth

To experimentally confirm the deeper probing depth of MCWG-based imaging compared to conventional SPRI, 10 μm diameter polystyrene microbeads (Polysciences Inc., USA) were seeded on the surface of MCWG and SPR chips. Because the volume of the beads extends well beyond the penetration depths of the SPRI and MCWG modes and because of the high curvature of the bead shapes, the circular "shadow" cast by the beads on the surface will vary significantly according to penetration depth. As a result, the apparent bead size as measured by the two imaging modalities differ according to their respective penetration depths.

Optics EXPRESS

For proper sedimentation of the beads on the chip surfaces, a drop of bead dilution in water was first deposited on the surface with a micropipette followed by evaporation of the water using a hotplate. After evaporation, the chips were mounted in the microscope system and the chip surfaces were re-immersed in distilled water for imaging, with the beads remaining firmly adhered to the chip surface. Brightfield, SPRI (λ = 633 nm), and MCWG images (λ = 470 nm) from a typical experiment are shown in Fig. 6.

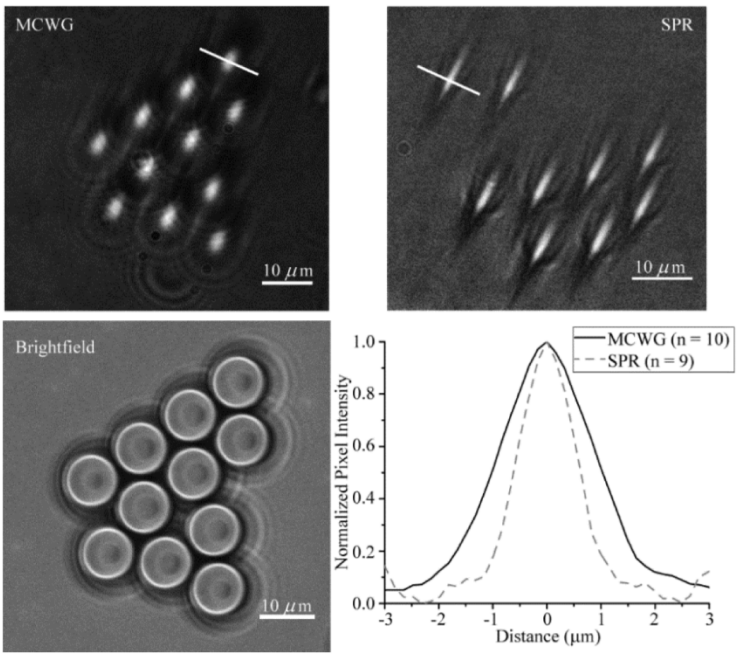

Fig. 6. Images of 10 um diameter polystyrene microbeads on the chip surface showing the effect of probing depth differences between MCWG and SPRI: TOP/LEFT: MCWG image (0.22 μm core, λ = 470 nm), TOP/RIGHT: SPRI (Au/water interface, λ = 633 nm), BOTTOM/LEFT: brightfield image. BOTTOM/RIGHT: plot of average bead image intensity profiles along the direction normal to light propagation (see example line overlays in two top images): the FWHM are 1.98 ± 0.19 μm and 1.18 ± 0.09 μm for the MCWG and SPRI bead images, respectively.

Because of the deeper penetration depth, the beads appear larger in the MCWG images compared to SPRI, as expected. Note that the "blurring artefact" caused by the finite attenuation distance in the direction of propagation is clearly visible in the two top images, as well as additional diffraction effects. To quantify the difference between the two imaging modalities, the average full widths at half maximum (FWHM) of the individual bead image profiles normal to the direction of light propagation were calculated across all imaged beads in both images (the example line overlays in the top images show the distance over which the individual bead image profiles were characterized). As seen in the plot of Fig. 6-BOTTOM/RIGHT, the FWHM for the MCWG bead images (1.98 ± 0.19 μm) is almost twice that for the SPRI bead images (1.18 ± 0.09 μm), confirming the deeper probing depth of MCWG. Note that these values are about half that predicted from a simple model based on the Fresnel equations evaluated at separate points in the plane of the surface according to the height of the bead/water interface at that location. The differences between the modeled and measured values are most likely due to the fact that the Fresnel equations model a stack of layers of infinite extent whereas the high curvature of the beads enables only a partial coupling of the excitation light to the guided modes at any point.

Optics EXPRESS

4.3 Imaging of living cells

To demonstrate the performance of MCWG for live cell imaging, adherent human embryotic kidney cells (HEK-293) were cultured directly on the KMPR chip surfaces. The cells were visualized simultaneously in the system with brightfield microscopy from the topside and with MCWG-based microscopy from the underside. Typical results are shown in Fig. 7. Since the cells are mostly transparent to visible light, little contrast is observed in the brightfield image (Fig. 7-BOTTOM/LEFT) though the image shows that the cells are well adhered and spread out on the surface. The contours of the 4 cells in the field of view are indicated by dotted lines. A pair of corresponding MCWG images acquired using orthogonal directions of light propagation (Fig. 7-TOP LEFT&RIGHT, arrows indicate directions of propagation) clearly show the 4 cells.

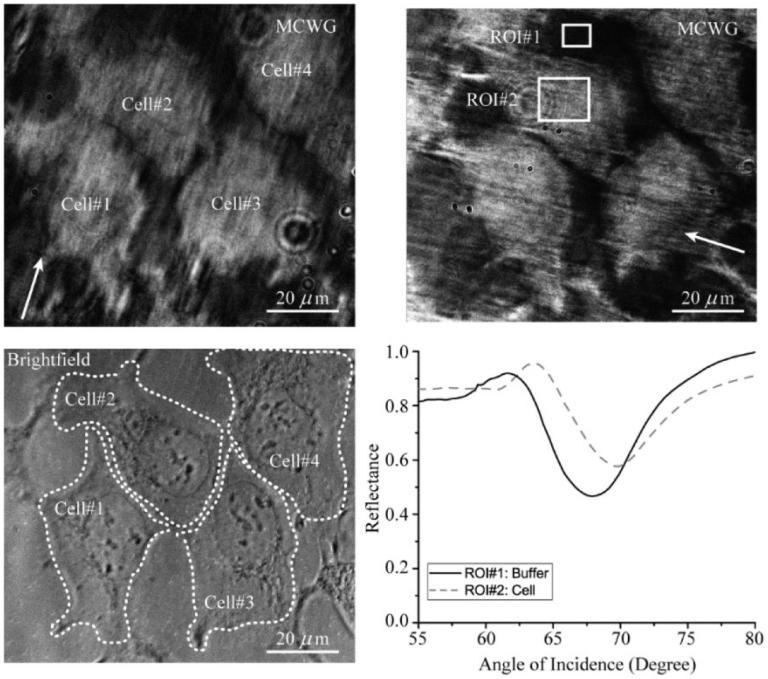

Fig. 7. Simultaneous brightfield and MCWG-based imaging of live HEK-293 cells cultured directly on the KMPR surface of a MCWG chip. TOP: MCWG-based reflectivity images for orthogonal light propagation directions acquired at 67.55° incidence angle (propagation directions indicated by arrows). BOTTOM/LEFT: Brightfield image showing the contours of the 4 cells in the field of view. BOTTOM/RIGHT: average reflectivity as a function of incidence angle from the two ROIs shown in MCWG images. ROI#1: extra-cellular medium, ROI#2: intra-cellular medium.

Indeed, since the intracellular structures in the HEK-293 cells (membrane, cytoskeletal components, and organelles) have a higher refractive index than the intra- and extra-cellular fluid, the resulting heterogeneous refractive index distribution gives rise to high-contrast MCWG-based images. The HEK-293 cells express various fibrous cytoskeleton components (e.g. actin) to maintain shape and integrity. Some of these subcellular structures will randomly be aligned with the direction of light propagation in which case their diameter can be resolved while their overall length will appear blurred due to the finite attenuation distance (diagonal line artefacts in the MCWG images).

Two regions of interest (ROI) were selected in the MCWG images as outlined by rectangular overlays: one corresponding to an area of the surface exposed to a buffer solution only and one encompassed by a cell body. Figure 7-BOTTOM/RIGHT shows measurements

Optics EXPRESS

of average reflectivity as a function of incidence angle from both ROIs, where the optimal coupling angle differs between the two (ROI#1: 67.86°, ROI#2: 69.88°) due to the difference in average refractive index. Interestingly, the presence of the cell not only shifts the angular position of the minimum coupling angle but also increases the value of the reflectance minimum. This effect is due to the fact that the intra-cellular environment is electromagnetically "lossy" due to scattering of the evanescent field by subcellular structures and organelles. Indeed, our group and others have shown that biological cells must be modeled as objects with complex refractive indices (n = 1.38 + i0.011 for ROI#2, determined by fitting to a Fresnel equations model) [13,36].

5. Conclusion

In this work, we have shown that MCWG-based microscopy is an effective and flexible method for high-resolution evanescent wave imaging. In particular, imaging using the MCWG TM0 mode at λ = 470 nm operating near cutoff (waveguide core thickness of 220 nm) is advantageous because of its deep probing depth (0.62 μm), good imaging spatial resolution (~5 μm), and high sensitivity (96 RIU^{-1}). While SPR is capable of higher spatial resolution at short wavelengths and LR-SPR can achieve deeper probing depth, MCWG-based microscopy offers the best compromise between spatial resolution and probing depth for imaging relatively thick biological objects such as cells or bacteria.

Acknowledgments

This work was supported by the Natural Sciences and Engineering Research Council of Canada (NSERC) (MG, PGC) and the Canadian Institutes of Health Research (CIHR) (MG, PGC). TS was supported by a doctoral scholarship from the Fonds de recherche du Québec – Nature et technologies (FRQNT).